Observing the linked depletion of dust and CO gas at 0.1-10 au in disks of intermediate-mass stars

A. Banzatti, A. Garufi, M. Kama, M. Benisty, S. Brittain, K. M. Pontoppidan, J. Rayner

A&A 609, L2 (2018)
https://doi.org/10.1051/0004-6361/201732034

Astronomy & Astrophysics

Letter to the Editor

Observing the linked depletion of dust and CO gas at 0.1–10 au in disks of intermediate-mass stars

A. Banzatti[1], A. Garufi[2], M. Kama[3], M. Benisty[4,5], S. Brittain[6], K. M. Pontoppidan[7], and J. Rayner[8]

[1] Lunar and Planetary Laboratory, The University of Arizona, Tucson, AZ 85721, USA
e-mail: banzatti@lpl.arizona.edu
[2] Universidad Autonónoma de Madrid, Dpto. Física Teórica, Facultad de Ciencias, Campus de Cantoblanco, 28049 Madrid, Spain
[3] Institute of Astronomy, Madingley Rd, Cambridge CB3 0HA, UK
[4] Unidad Mixta Internacional Franco-Chilena de Astronomía, CNRS/INSU UMI 3386 and Departamento de Astronomía, Universidad de Chile, Casilla 36-D, Santiago, Chile
[5] Univ. Grenoble Alpes, CNRS, IPAG, 38000 Grenoble, France
[6] Department of Physics & Astronomy, 118 Kinard Laboratory, Clemson University, Clemson, SC, USA
[7] Space Telescope Science Institute, 3700 San Martin Drive, Baltimore, MD 21218, USA
[8] University of Hawaii, 2680 Woodlawn Drive, Honolulu, HI 96822-0345, USA

Received 3 October 2017 / Accepted 26 November 2017

ABSTRACT

We report on the discovery of correlations between dust and CO gas tracers of the 0.1–10 au region in planet-forming disks around young intermediate-mass stars. The abundance of refractory elements on stellar photospheres decreases as the location of hot CO gas emission recedes to larger disk radii, and as the near-infrared excess emission from hot dust in the inner disk decreases. The linked behavior between these observables demonstrates that the recession of infrared CO emission to larger disk radii traces an inner disk region where dust is being depleted. We also find that Herbig disk cavities have either low (~5–10%) or high (~20–35%) near-infrared excess, a dichotomy that has not been captured by the classic definition of "pre-transitional" disks.

Key words. protoplanetary disks – stars: pre-main sequence – stars: variables: T Tauri, Herbig Ae/Be – planets and satellites: formation

1. Introduction

The vast majority of exoplanets discovered so far lies at less than 3 au from the central star, with super-Earths abundant well inside 1 au (e.g., Petigura et al. 2013). Planets of up to a few Earth masses could form in situ (e.g., Hansen & Murray 2012), while giant planets most probably migrate inward from beyond a few au (e.g., Kley & Nelson 2012). Whether exoplanets form or migrate where they are detected, the effect of the structure and evolution of protoplanetary disks at 0.1–10 au is expected by all models to be fundamental in shaping planetary systems.

First measurements on the evolution of inner disks came from spatially unresolved observations of spectral energy distributions (SEDs), which in some disks show a lower infrared (IR) flux that was attributed to a deficit of hot inner material (Strom et al. 1989). This deficit has been interpreted as due to inner holes ("transitional" disks) or gaps ("pre-transitional" disks), depending on the level of near-IR flux related to an inner dust belt inside the cavity (Espaillat et al. 2007). Modern imaging techniques, probing disk radii of $\gtrsim$5 au, have confirmed the existence of >10 au wide cavities in several disks, depleted of dust particles of up to centimeter sizes (e.g., Andrews et al. 2011). A leading theory for the origin of these cavities is disk clearing by planets, exo-Jupiters, but possibly also super-Earths (e.g., Pinilla et al. 2012; Fung & Chiang 2017). Inner disks can be dispersed by winds as well, although observations cannot yet be fully reconciled in any photoevaporative or planet-disk interaction models (Owen 2016). In disks around young intermediate-mass stars (Herbig Ae/Be stars), the far-IR excess of the SED, tracing colder material at larger radii, has been adopted by Meeus et al. (2001) to classify disks into Group I (GI, with high excess) and Group II (GII, with moderate excess). The current understanding of this empirical classification is that it reflects a different disk structure, with GI having a large disk cavity that allows the irradiation of the disk at $\gtrsim$10 au, and GII having no or at most small inner cavities (Maaskant et al. 2013; Menu et al. 2015; Honda et al. 2015; Garufi et al. 2017).

While near-IR and millimeter imaging now reveal increasing detail in global disk structures (e.g., ALMA Partnership et al. 2015; Benisty et al. 2015), information on the inner disk structure at $\lesssim$5 au can only be obtained from optical and near-IR spectroscopy and near-IR interferometry. Recently, independent studies have found new evidence in dust and gas tracers pointing in the direction of depletion processes in these inner disk regions (Kama et al. 2015; Banzatti & Pontoppidan 2015). By combining these independent datasets (Sect. 2), we report in this work on the discovery of a linked behavior between observables of CO gas and dust in inner disks (Sect. 3). This behavior demonstrates a strong link between molecular gas and dust, providing an important framework for better understanding the evolving structure of planet-forming regions at $\lesssim$10 au (Sect. 4).

2. Sample and measurements

The three independent datasets combined in this analysis are the orbital radius and excitation of rovibrational CO emission

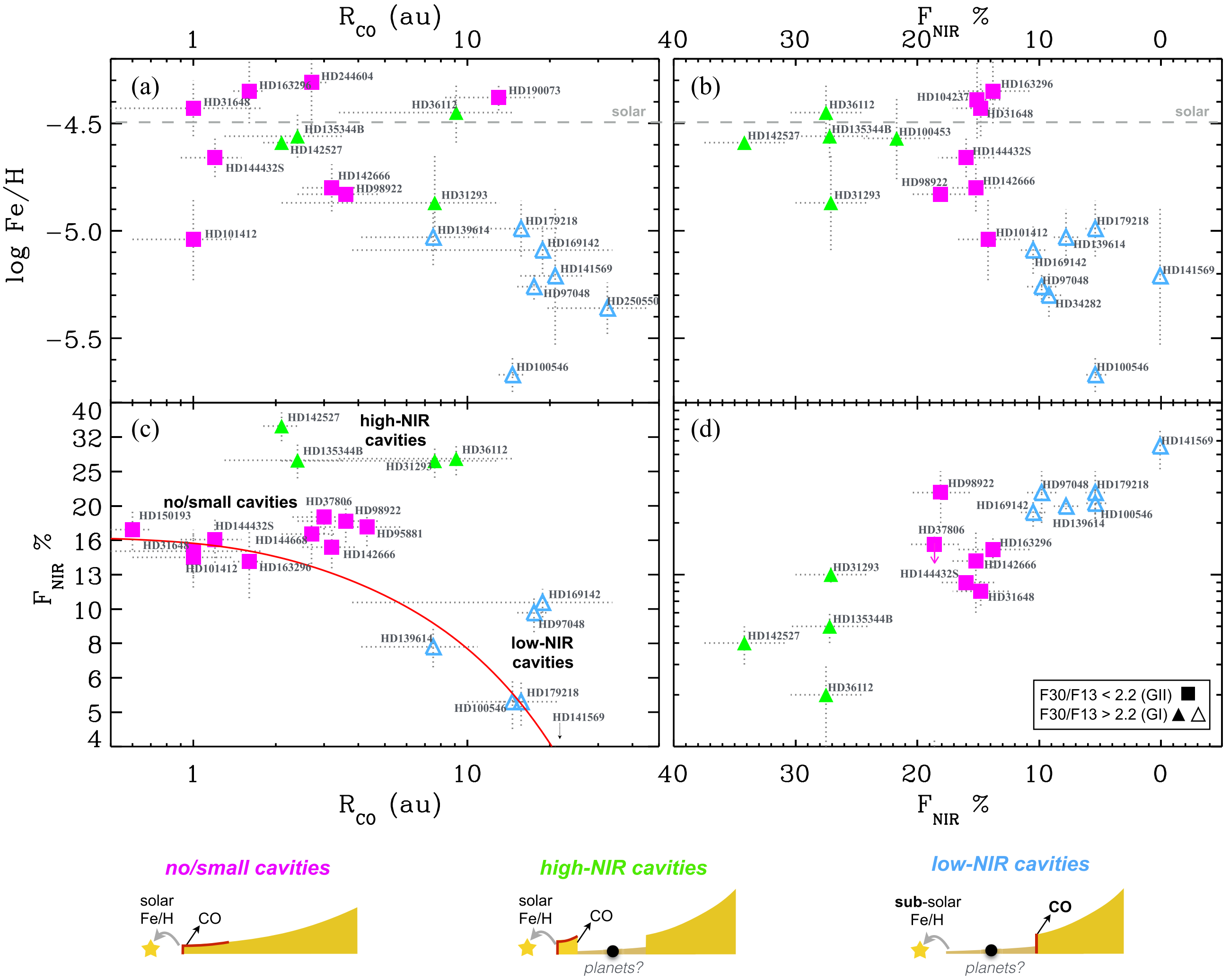

Fig. 1. Linked behavior between the datasets combined in this work. *a)* Fe/H vs R_{co}. *b)* Fe/H vs F_{NIR}. *c)* F_{NIR} vs R_{co}. *d)* $v2/v1$ vs F_{NIR}. The red curve shows a parametric model of the decrease of F_{NIR} with increasing size of an inner cavity (see text for details). The three disk categories identified in the multi-dimensional parameter space are illustrated to the bottom. Dust is shown in yellow, and we mark the approximate location of infrared CO emission. Dust depletion is shown as a thinner yellow layer of residual dust, and dust layers that dominate the observed F_{NIR} are marked in red. GII disks are shown as magenta squares, high-NIR GI disks as green triangles, low-NIR GI disks as cyan (empty) triangles.

(Sect. 2.1), the iron abundance Fe/H as measured on stellar photospheres (Sect. 2.2), and the near-IR excess over the stellar flux in the SED (Sect. 2.3). The sample includes the majority of well-known Herbig Ae/Be stars within 200 pc, together with some at larger distances: 26 late-B, A, and F stars with temperatures T_{eff} between 6500 and 11 000 K, masses between 1.5 and 4 $M_{\odot}$, and ages between 1 and 10 Myr. The sample is composed evenly by GI and GII disks (13 each), and we adopt the classification criterion from Garufi et al. (2017), where the flux ratio at 30 and 13 μm is used to separate GI disks (with $F30/F13 > 2.2$) from GII disks (with $F30/F13 < 2.2$, where 2.2 is the ratio for a flat SED). All three datasets are available for 16 of these objects, while only two are available for the other 10 (Table A.1).

2.1. Rovibrational CO emission

Spectrally resolved emission line profiles provide information on gas kinematics in protoplanetary disks. Rovibrational CO emission at 4.7–4.8 μm was used to estimate a characteristic orbital radius of hot/warm (~300–1500 K) CO gas in Keplerian rotation in a disk, as $R_{co} = (2 \sin i / FWHM_{co})^2 GM_{\star}$, where $M_{\star}$ is the stellar mass and i the disk inclination. As a characteristic gas velocity, we took the CO line velocity at the half width at half maximum ($FWHM_{co}/2$) as in Banzatti & Pontoppidan (2015). For the disk inclinations, we adopted values from the near-IR interferometric survey by Lazareff et al. (2017), which probe inner disks at <10 au. The 1σ errors on R_{co} were propagated from the uncertainties on stellar masses, CO line widths, and disk inclinations, and they are dominated by the disk inclination uncertainties. Most CO spectra have been published previously, except for four disks that were newly observed with IRTF-ISHELL (see Appendix B). Another measured property of CO emission is the flux ratio between rovibrational lines from the second and first vibrational levels. The ratio $v2/v1$ is a sensitive tracer of the type of CO excitation (e.g., Brittain et al. 2003, 2007; Thi et al. 2013): UV-pumping populates high vibrational states first (producing higher $v2/v1$), while IR-pumping and collisional excitation populate low states first (producing lower $v2/v1$).

2.2. Refractory abundance on stellar photosphere

Modeling of high-resolution optical spectra enables measuring elemental abundances on stellar photospheres. We used the stellar Fe/H compilation from Kama et al. (2015), including mostly values from Folsom et al. (2012). The very shallow surface convection zone in stars with $T_{\rm eff} \gtrsim 7500$ K inhibits mixing with the bulk of the stellar envelope and keeps accreted material visible on the photosphere for ~1 Myr. The Fe/H measurements in Herbig Ae/Be stars have recently been found to correlate with the presence or absence of dust cavities detected by millimeter interferometry imaging, suggesting that the stellar photospheres keep an imprint of the dust/gas ratio of their inner disks through the accreted material (Kama et al. 2015). Two stars in the sample have $T_{\rm eff}$ lower than 7500 K, HD142527 and HD135344B; these stars are likely mixing the accreted material more efficiently than the rest of the sample.

2.3. Near-infrared excess

A traditional probe of hot dust in inner disks is the near-IR excess (e.g., Dominik et al. 2003). We estimated the fractional $F_{\rm NIR} = F({\rm NIR})/F_\star$ for our entire sample to ensure an homogeneous procedure, and found values consistent with those estimated in previous work. We collected the *BVRJHK* photometry, along with the WISE fluxes at 3.6 and 4.5 μm and dereddened by means of the extinction $A_{\rm V}$ available from the literature ($A_{\rm V} < 0.5$ mag for most of this sample; Meeus et al. 2012). A PHOENIX model of the stellar photosphere (Hauschildt et al. 1999) with the literature stellar temperature and metallicity and a surface gravity $\log(g) = -4.0$ was employed for each source and scaled to the dereddened V magnitude for each source. The near-IR excess $F_{\rm NIR}$ was measured by integrating the observed flux exceeding the stellar flux between 1.2 and 4.5 μm. These values were then divided by the total stellar flux $F_\star$ from the model. The 1σ errors on $F_{\rm NIR}$, propagated from the uncertainties on $T_{\rm eff}$ and an assumed uncertainty of 0.2 mag in $A_{\rm V}$, are typically 13% (median value), and always $\lesssim$20% (Table A.1).

3. Linked behavior between the datasets

The datasets combined in this work show a linked behavior in the multi-dimensional parameter space illustrated in the four panels of Fig. 1. The correlation between Fe/H and $R_{\rm co}$ demonstrates a link between two observables that could in principle be independent of each other: iron is depleted from the stellar photospheres as $R_{\rm co}$ recedes to larger radii in their inner disks. GII disks have, on average, smaller $R_{\rm co}$ and higher Fe/H, while GI disks have the opposite, larger $R_{\rm co}$ and lower Fe/H. A group of GI disks overlaps with GII disks at intermediate values of $R_{\rm co}$.

$F_{\rm NIR}$ values are found to lie between 5% and 34%, with only one disk showing a value as low as 0.08% (HD141569, see Sect. 4.2). All GII disks show $F_{\rm NIR}$ in the narrow range between 14% and 19%. GI disks instead span a wider range of $F_{\rm NIR}$, some with lower values than the GII (5–11%) and some with higher values (22–34%, see also Garufi et al. 2017). Overall, disks with larger $R_{\rm co}$ have lower $F_{\rm NIR}$ and Fe/H, although without a simple monotonic relation between $R_{\rm co}$ and $F_{\rm NIR}$. In addition, there is a strong linear anticorrelation between $F_{\rm NIR}$ and the CO vibrational ratio $v2/v1$ (Fig. 1d).

Three categories of disks can be identified as based on inner disk observables (Fig. 1 and Table 1). Beyond nomenclature or classification intents, we can understand the evolving properties of inner disks more comprehensively by identifying which observable properties separate out in this multi-dimensional space. Interestingly, the GI disks in the sample are split into two very distinct parts of the parameter space, and we refer to them as "high-NIR" and "low-NIR" GI disks to identify the different behavior of inner disk observables. This dichotomy in $F_{\rm NIR}$ values of GI disks is strongly segregated, with the Kolmogorov–Smirnov (KS) two-sided test highly rejecting the hypothesis that they may be drawn from a same parent distribution (probability of <1%). The three categories are instead not separated in terms of stellar temperature, mass, luminosity, or age, nor in mass accretion rates (see Fig. A.1), and no correlation is found between these parameters and $R_{\rm co}$, $F_{\rm NIR}$, or Fe/H, suggesting that the measured behavior of inner disk observables cannot be attributed to these parameters.

Table 1. Median values for the three disk categories as in Fig. A.1.

log(Fe/H)	$R_{\rm co}$	$F_{\rm NIR}$	$v2/v1$	$F30/F13$	Cavity?
−4.4	3 au	16%	0.12	1.2	No/small
−4.6	5 au	27%	0.05	5	"High-NIR"
−5.2	18 au	8%	0.27	5	"Low-NIR"

The linked behavior between inner disk tracers of CO and dust may be produced by a scenario where as dust is depleted (as shown by the decrease in $F_{\rm NIR}$ and Fe/H), CO gas is depleted as well (CO emission at high velocity decreases, $FWHM_{\rm co}$ shrinks, and $R_{\rm co}$ moves to larger disk radii). As a simple test of whether a linked depletion of CO gas and dust from the inner disk may globally reproduce the observed trends, we adopted a parametric description of an inner disk structure in hydrostatic equilibrium, as based on work by Kama et al. (2009) and summarized in Appendix C. The disk temperature decreases with disk radius as $r^{-0.5}$, and we explored how $F_{\rm NIR}$ decreases as the radius of the innermost dust ($R_{\rm dust}$) was sequentially increased to mimic the formation of an inner hole.

A decrease of $F_{\rm NIR}$ with increasing hole size (red curve in Fig. 1c) is naturally produced by a decreasing temperature of the emitting dust, as hotter dust at smaller radii is removed. In this scenario, $R_{\rm co}$ could trace the size of an inner dust-depleted disk region, as suggested from previous observations (Brittain et al. 2003, 2007). When Keplerian line profiles are modeled assuming a power-law radial brightness (e.g., Salyk et al. 2011), $R_{\rm co}$ as defined here can be several times larger than $R_{\rm dust}$ (taken as the innermost radius where CO gas can also exist). The model curve in Fig. 1c shows $R_{\rm dust}$ multiplied by 7, by assuming the median scaling factor between $R_{\rm co}$ values and the $R_{\rm dust}$ values from Lazareff et al. (2017) for this sample. By assuming devoid inner holes, this simple model provides only a trend of the lower boundary to the data points in the figure. Reproducing the high near-IR excess of some Herbig disks has been a long-standing modeling challenge that is still unsolved (see, e.g., Dullemond et al. 2001; Vinković et al. 2006). New modeling efforts could be devoted to studying how $F_{\rm NIR}$ can be increased toward values measured in the high-NIR GI disks (25–35%) by keeping an inner residual dust component while inner cavities are forming at larger disk radii. Such a structure is supported by recent observations of these disks, as discussed below.

4. Discussion

4.1. Dust and gas depletion in the inner disk regions

The behavior of inner disk observables presented in this work can be affected by processes that involve different modifications to the radial distributions of dust and gas. Beyond the scope of this work, quantification of these processes requires explorations with sophisticated thermo-chemical models of disks, which have only recently started to be applied to disks with inner cavities (e.g., Bruderer 2013). We advocate in this work a strong empirical evidence for a link in the evolution of dust and molecular gas in planet-forming regions, extending to inner disk radii smaller than can be spatially resolved by ALMA.

Sub-solar Fe/H (and other refractories) on radiative stellar photospheres have long been suggested to be linked to dust-depleted material accreted onto the star (e.g., Venn & Lambert 1990), but it was unclear why only some Herbig Ae/Be stars exhibit a depletion of refractories (Folsom et al. 2012). Kama et al. (2015) showed that sub-solar refractory abundances in Herbig stars correlate with the presence of a large (>10 au) dust cavity in their disks, pointing out that the depletion of dust grains in the inner regions of transitional disks would naturally explain a lack of refractories in the accreting material. The correlation between Fe/H and $F_{\rm NIR}$ shown here demonstrates that a link exists between refractory abundances on stellar photospheres and the properties of dusty inner disks at <10 au. To decrease both Fe/H and $F_{\rm NIR}$, dust must be depleted from both the accretion flow and from the inner disk. Potential processes include 1) dust grain growth/inclusion into solids larger than ≫1 mm (pebbles and planetesimals) that decouple from the accreted gas and emit less efficiently in the infrared, 2) physical decoupling of inner and outer disk, where the resupply of inner disk dust by inward drift from the outer disk is inhibited (see, e.g., discussions in Andrews et al. 2011; Kama et al. 2015).

The survival of CO gas in a dust-depleted cavity of Herbig disks was specifically investigated by Bruderer (2013). The study showed that as long as inner disks are still gas rich (N(H_2) ≈ 10^{27} cm^{-2} at <1 au), the radial distribution of CO gas does not depend on the presence of dust, as the density of CO molecules is well above the column needed to self-shield from UV photodissociation (Visser et al. 2009). When instead the total gas content in the inner disk is decreased by at least four orders of magnitude, reaching column densities where UV photodissociation of CO becomes relevant, the survival of CO is closely linked to the presence of shielding dust. Specifically, in a dust- and gas-depleted cavity, the CO column density decreases by orders of magnitude by UV photodissociation inside the cavity when a residual inner dust belt is removed. In this situation, $R_{\rm co}$ will shift to larger radii as the dust is depleted from the innermost disk radii. In the framework of this modeling, the linked behavior between dust and CO gas observables suggests that low-NIR GI disks with large $R_{\rm co}$ may be in a gas-depleted regime. Gas depletion factors of 10^2–10^4 have been supported by recent analyses of millimeter CO emission in some of these disks, as imaged by ALMA (van der Marel et al. 2016).

4.2. Dichotomy of inner disk cavities

The net separation between high-NIR and low-NIR GI disks suggests that large inner disk cavities have two possible structures. Their properties are at the opposite extremes of those of GII disks with no/small cavities (Figs. 1 and 2). This dichotomy once again suggests a strong link between dust and gas, consistent with the inner disk structure discussed above in thermo-chemical modeling work: a residual inner dust component (high $F_{\rm NIR}$) may allow for UV-shielded and vibrationally colder CO gas to survive in a dust-free cavity at larger radii ($v2/v1$ < 0.1 in high-NIR disks), while its removal would allow for an efficient UV photodissociation of CO gas inside the dust cavity and for UV pumping at the cavity wall ($v2/v1$ ∼ 0.3 in low-NIR disks).

We note that $F_{\rm NIR}$ does not show a monotonic relation with $F30/F13$ (Fig. 2) and that the 10 μm silicate emission is found in disks with cavities regardless of the measured level

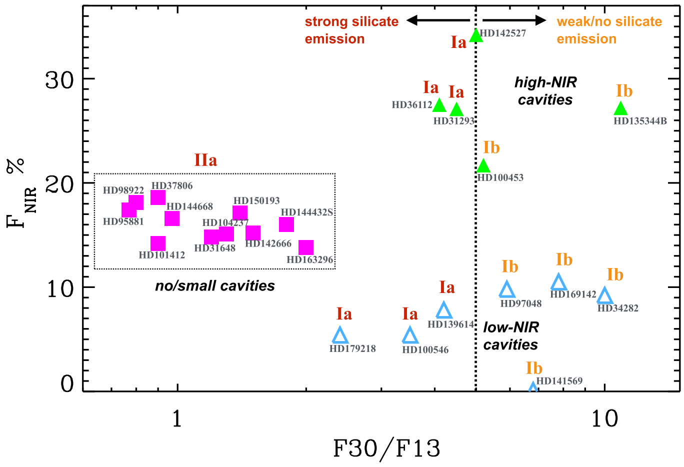

Fig. 2. $F_{\rm NIR}$ and $F30/F13$ for this sample of Herbig disks, highlighting the three classes as in Fig 1. Following Meeus et al. (2001), we mark disks where the 10 μm silicate emission has been detected ("IIa" and "Ia") or not ("Ib"); we keep the color-coding for the Ia/Ib labels from Maaskant et al. (2013) to facilitate comparison to that work. Maaskant et al. (2013) showed that silicate emission is tightly related to the $F30/F13$ ratio; instead, $F_{\rm NIR}$ is unrelated (Sect. 4.2).

of $F_{\rm NIR}$. While $F30/F13$ traces the depletion of intermediate disk regions where the warm (∼200–400 K) silicate emission is produced (Maaskant et al. 2013), $F_{\rm NIR}$ in the high-NIR disks must be produced by a hotter disk region closer to the star. We also note that no Herbig disk in this sample has $F_{\rm NIR}$ ∼ 0, except for HD141569, which has been proposed to be globally dispersing its gas toward the debris disk phase (e.g., White et al. 2016). This suggests that inner cavities in Herbig disks are depleted but never completely devoid of material, consistent with residual dust detected at the sublimation radius by NIR interferometry (Lazareff et al. 2017) and with significant accretion rates measured even in low-NIR disks. The moderate/high accretion rates measured in some stars with large inner disk cavities currently provide one of the main open problems in understanding the structure and origin of disk cavities (e.g., Owen 2016; Ercolano & Pascucci 2017); interestingly, CO gas depletion in the disk has recently been proposed as a potential solution (Ercolano et al. 2018).

The nature of a hot inner dust component in high-NIR cavities remains to be determined. Studies have investigated how $F_{\rm NIR}$ can be increased by i) increasing the inner rim scale-height by thermal or magnetic processes (Dullemond et al. 2001; Flock et al. 2017), ii) a dusty wind launched close to the dust sublimation radius (e.g., HD31293 as modeled by Bans & Königl 2012), iii) misaligned inner disks with warps induced by a gap-opening companion (Owen & Lai 2017). All these scenarios invoke vertically extended inner dusty structures that will have effects on CO gas excitation, and still need to be investigated by thermo-chemical models. Intriguingly, the presence of misaligned inner disks has been linked to the presence of shadows and spirals at larger disk radii (e.g., Montesinos et al. 2016; Min et al. 2017), which have been imaged in all high-NIR GI disks (Benisty et al. 2015; Stolker et al. 2016; Avenhaus et al. 2017; Benisty et al. 2017; Tang et al. 2017).

We highlight that the dichotomy of inner disk cavities presented in this work has not been captured by the classic definition of a "pre-transitional" disk, as low-/high-NIR GI disks have been indistinguishably classified "pre-transitional" (Espaillat et al. 2014). A combination of multiple tracers of dust and gas in

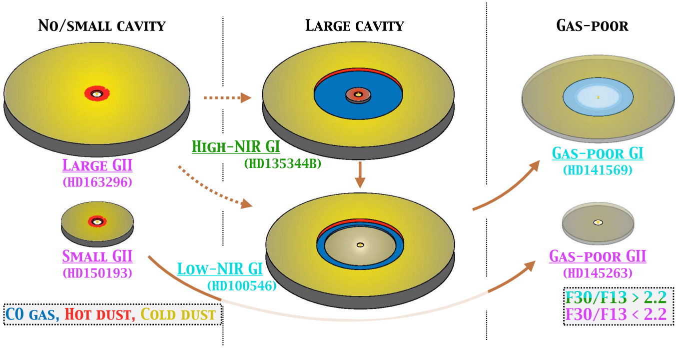

Fig. 3. Evolutionary paths that appear possible by combining this work and the analysis of Garufi et al. (2017). The dichotomy in inner disk cavities is shown at the center: high-NIR cavities have a residual inner dust component, possibly a belt/warp, that shields UV radiation and enables CO (vibrationally cold) to survive into the cavity; low-NIR cavities are instead dust- and gas-depleted, and CO (here vibrationally hot) is detected only close to the cavity wall.

inner and outer disk regions is needed to refine previous concepts of "(pre-)transitional" disks into a better understanding of their structure and evolutionary phase. While some GII disks are already too small in radius and low in mass to ever show the properties of GI disks (e.g., HD150193 and HD145263; see Garufi et al. 2017), it is possible that others are still overall large and massive enough to do so, if they eventually form a large inner cavity (e.g., the GII disk HD163296; Fig. 3). As argued in previous work, this suggests that at least two paths of disk evolution may be sampled by current observations. The observed dichotomy of GI cavities may instead suggest a potential "on/off" behavior of the hot inner dust component, where as soon as an inner dust belt/warp is removed, R_{co} abruptly recedes to $\gtrsim$10 au due to the destruction of residual CO gas by UV photodissociation in a dust- and gas-depleted cavity (Sect. 4.1).

5. Conclusions

From the combination of three independent tracers of dust and CO gas in the inner disks of intermediate-mass stars, we conclude that

- the recession of NIR CO emission to larger disk radii traces dust depletion in inner disks at ≈0.1–10 au, providing key measurements of disk evolution in inner regions beyond reach of direct-imaging techniques; based on recent thermo-chemical modeling (Bruderer 2013), this behavior seems to imply that these disk cavities may also be gas depleted;
- the multi-dimensional space of the several observables now available suggests that large cavities in Herbig disks form with either low (~5–10%) or high (~20–35%) NIR excess, a dichotomy that was not captured by the classic definition of "pre-transitional" disks; high-NIR GI disks seem to have residual inner dust belts/warps that have recently been inferred also from shadows and spirals at larger disk radii.

Acknowledgements. We thank A. Carmona for providing CO data of HD169142, and acknowledge helpful feedback and discussions with A. Bosman, G. Dipierro, U. Gorti, G. Mulders, P. Pinilla, and E. van Dishoeck. We also thank the anonymous referee for suggestions that helped improve the presentation of this work. M.B. acknowledges funding from ANR of France under contract number ANR-16-CE31-0013 (Planet Forming Disks). This work is partly based on observations obtained at the Infrared Telescope Facility, which is operated by the University of Hawaii under contract NNH14CK55B with the National Aeronautics and Space Administration. This research has made use of the VizieR catalogue, CDS, Strasbourg, France (Ochsenbein et al. 2000).

References

ALMA Partnership, Brogan, C. L., Pérez, L. M., et al. 2015, ApJ, 808, L3
Andrews, S. M., Wilner, D. J., Espaillat, C., et al. 2011, ApJ, 732, 42
Avenhaus, H., Quanz, S. P., Schmid, H. M., et al. 2017, AJ, 154, 33
Bans, A., & Königl, A. 2012, ApJ, 758, 100
Banzatti, A., & Pontoppidan, K. M. 2015, ApJ, 809, 167
Banzatti, A., Pontoppidan, K. M., Salyk, C., et al. 2017, ApJ, 834, 152
Benisty, M., Juhasz, A., Boccaletti, A., et al. 2015, A&A, 578, L6
Benisty, M., Stolker, T., Pohl, A., et al. 2017, A&A, 597, A42
Brittain, S. D., Rettig, T. W., Simon, T., et al. 2003, ApJ, 588, 535
Brittain, S. D., Simon, T., Najita, J. R., & Rettig, T. W. 2007, ApJ, 659, 685
Bruderer, S. 2013, A&A, 559, A46
Dominik, C., Dullemond, C. P., Waters, L. B. F. M., & Walch, S. 2003, A&A, 398, 607
Dullemond, C. P., Dominik, C., & Natta, A. 2001, ApJ, 560, 957
Ercolano, B., & Pascucci, I. 2017, Roy. Soc. Open Sci., 4, 170114
Ercolano, B., Weber, M. L., & Owen, J. E. 2018, MNRAS, 473, L64
Espaillat, C., Calvet, N., D'Alessio, P., et al. 2007, ApJ, 670, L135
Espaillat, C., Muzerolle, J., Najita, J., et al. 2014, Protostars and Planets VI, 497
Fairlamb, J. R., Oudmaijer, R. D., Mendigutía, I., Ilee, J. D., & van den Ancker, M. E. 2015, MNRAS, 453, 976
Fedele, D., van den Ancker, M. E., Acke, B., et al. 2008, A&A, 491, 809
Flock, M., Fromang, S., Turner, N. J., & Benisty, M. 2017, ApJ, 835, 230
Folsom, C. P., Bagnulo, S., Wade, G. A., et al. 2012, MNRAS, 422, 2072
Fung, J., & Chiang, E. 2017, ApJ, 839, 100
Garufi, A., Meeus, G., Benisty, M., et al. 2017, A&A, 603, A21
Hansen, B. M. S., & Murray, N. 2012, ApJ, 751, 158
Hauschildt, P. H., Allard, F., & Baron, E. 1999, ApJ, 512, 377
Honda, M., Maaskant, K., Okamoto, Y. K., et al. 2015, ApJ, 804, 143
Kama, M., Min, M., & Dominik, C. 2009, A&A, 506, 1199
Kama, M., Folsom, C. P., & Pinilla, P. 2015, A&A, 582, L10
Kley, W., & Nelson, R. P. 2012, ARA&A, 50, 211
Lazareff, B., Berger, J.-P., Kluska, J., et al. 2017, A&A, 599, A85
Maaskant, K. M., Honda, M., Waters, L. B. F. M., et al. 2013, A&A, 555, A64
Maaskant, K. M., Min, M., Waters, L. B. F. M., & Tielens, A. G. G. M. 2014, A&A, 563, A78
Meeus, G., Waters, L. B. F. M., Bouwman, J., et al. 2001, A&A, 365, 476
Meeus, G., Montesinos, B., Mendigutía, I., et al. 2012, A&A, 544, A78
Menu, J., van Boekel, R., Henning, T., et al. 2015, A&A, 581, A107
Min, M., Dullemond, C. P., Dominik, C., de Koter, A., & Hovenier, J. W. 2009, A&A, 497, 155
Min, M., Stolker, T., Dominik, C., & Benisty, M. 2017, A&A, 604, L10
Montesinos, M., Perez, S., Casassus, S., et al. 2016, ApJ, 823, L8
Ochsenbein, F., Bauer, P., & Marcout, J. 2000, A&AS, 143, 23
Owen, J. E. 2016, PASA, 33, e005
Owen, J. E., & Lai, D. 2017, MNRAS, 469, 2834
Petigura, E. A., Howard, A. W., & Marcy, G. W. 2013, PNAS, 110, 19273
Pinilla, P., Benisty, M., & Birnstiel, T. 2012, A&A, 545, A81
Rayner, J., Tokunaga, A., Jaffe, D., et al. 2016, Proc. SPIE, 9908, 990884
Salyk, C., Blake, G. A., Boogert, A. C. A., & Brown, J. M. 2011, ApJ, 743, 112
Stolker, T., Dominik, C., Avenhaus, H., et al. 2016, A&A, 595, A113
Stolker, T., Sitko, M., Lazareff, B., et al. 2017, ApJ, 849, 143
Strom, K. M., Strom, S. E., Edwards, S., Cabrit, S., & Skrutskie, M. F. 1989, AJ, 97, 1451
Tang, Y.-W., Guilloteau, S., Dutrey, A., et al. 2017, ApJ, 840, 32
Thi, W. F., Kamp, I., Woitke, P., et al. 2013, A&A, 551, A49
van der Marel, N., van Dishoeck, E. F., Bruderer, S., et al. 2016, A&A, 585, A58
van der Plas, G., van den Ancker, M. E., Waters, L. B. F. M., & Dominik, C. 2015, A&A, 574, A75
Venn, K. A., & Lambert, D. L. 1990, ApJ, 363, 234
Vinković, D., Ivezić, Ž., Jurkić, T., & Elitzur, M. 2006, ApJ, 636, 348
Visser, R., van Dishoeck, E. F., & Black, J. H. 2009, A&A, 503, 323
White, J. A., Boley, A. C., Hughes, A. M., et al. 2016, ApJ, 829, 6

Appendix A: The sample

The sample properties are reported in Table A.1 and Fig. A.1.

Table A.1. Sample properties, separated into the three disk categories discussed in the text.

Name	$T_{\rm eff}$ (K)	$M_\star$ ($M_\odot$)	$M_{\rm acc}$ ($M_\odot\,{\rm yr}^{-1}$)	log(Fe/H)	Incl (deg)	$FWHM_{\rm co}$ (km s^{-1})	$R_{\rm co}$ (au)	$v2/v1$	$F_{\rm NIR}$ (%)	$F30/F13$
HD31648	8800	2.1	−6.9	−4.43	39	55	1.0 (0.8)	0.08	14.8 (2.3)	1.2
HD37806	11 000	3.9	−6.3	–	41	45	3.0 (0.7)	<0.15	18.6 (2.0)	0.9
HD95881	9000	2.0	–	–	52	32	4.3 (1.4)	–	17.4 (2.1)	0.8
HD98922	10 500	4.0	–	−4.83	20	22	3.6 (1.2)	0.30	18.1 (2.4)	0.8
HD101412	8600	3.0	−7.0	−5.04	80	100	1.0 (0.4)	–	14.2 (2.6)	0.9
HD104237	8000	2.0	−6.7	−4.39	–	–	–	–	15.1 (1.9)	1.3
HD142666	7500	2.0	−7.8	−4.80	60	40	3.2 (0.7)	0.12	15.2 (2.0)	1.5
HD144432S	7400	2.0	−7.4	−4.66	25	32	1.2 (0.3)	0.09	16.0 (2.3)	1.8
HD144668	8500	2.5	−6.3	–	52	45	2.7 (0.6)	–	16.6 (3.0)	1.0
HD150193	9000	1.9	−7.5	–	32	54	0.6 (0.1)	–	17.1 (2.2)	1.4
HD163296	9200	2.3	−7.5	−4.35	48	53	1.6 (0.2)	0.14	13.8 (3.0)	2.0
HD190073	9230	2.9	−8.7	−4.38	31	14	13.0 (4.7)	0.30	–	0.8
HD244604	8700	2.8	−7.2	−4.31	55	49	2.7 (0.4)	<0.11	–	1.4
GII disks	8800	2.3	−7.2	−4.4	45	45	3	0.12	16	1.2
	(600)	(0.5)	(0.4)	(0.2)	(17)	(14)	(2)	(0.04)	(2)	(0.4)
HD31293	9800	2.5	−7.7	−4.87	24	14	7.6 (5.5)	0.10	27.1 (2.9)	4.5
HD36112	8200	2.8	−6.1	−4.45	49	25	9.1 (5.7)	0.02	27.5 (2.9)	4.1
HD100453	7250	1.5	−8.0	−4.57	49	–	–	–	21.7 (2.7)	5.2
HD135344B	6375	1.5	−7.4	−4.56	18	14	2.4 (1.1)	0.05	27.2 (3.1)	10.9
HD142527	6500	1.6	−7.5	−4.59	33	28	2.1 (0.3)	0.04	34.2 (3.3)	5.0
High-NIR GI	7300	2.0	−7.5	−4.6	33	20	5	0.05	27	5
	(1300)	(0.2)	(0.3)	(0.03)	(21)	(8)	(4)	(0.02)	(0.4)	(1)
HD34282	9500	1.9	−7.7	−5.30	66	–	–	–	9.2 (1.0)	10.0
HD97048	10 500	2.2	−6.8	−5.26	56	18	17.5 (2.3)	0.30	9.8 (1.2)	5.9
HD100546	10 400	2.3	−7.0	−5.67	46	17	14.6 (1.6)	0.26	5.4 (0.9)	3.5
HD139614	7600	1.7	−7.6	−5.03	32	15	7.5 (3.4)	0.25	7.8 (1.0)	4.2
HD141569	9800	2.4	−7.7	−5.21	53	16	20.9 (5.3)	0.56	0.08 (0.01)	6.8
HD169142	7500	1.7	−7.4	−5.09	23	7	18.8 (15.0)	0.23	10.5 (1.0)	7.8
HD179218	9640	3.1	−6.7	−4.99	49	20	15.7 (5.7)	0.30	5.4 (0.8)	2.4
HD250550	11 000	3.4	−5.6	−5.36	52	15	32.4 (12.8)	0.16	–	2.5
Low-NIR GI	9700	2.3	−7.2	−5.2	51	16	18	0.27	8	5
	(1100)	(0.7)	(0.7)	(0.2)	(7)	(2)	(4)	(0.09)	(4)	(3)

Notes. Median values and median absolute deviations (in parentheses) of all parameters are included below each disk category. Stellar temperatures and masses are from Folsom et al. (2012) and Fairlamb et al. (2015); accretion rates are from Fairlamb et al. (2015); Fe/H values are taken from the compilation in Kama et al. (2015). Inner disk inclinations are adopted from Lazareff et al. (2017), except for HD101412 (Fedele et al. 2008), HD141569 (White et al. 2016), and HD135344B (Stolker et al. 2017). CO line widths and vibrational ratios are taken from the compilation in Banzatti et al. (2017) and from this work, except for HD169142, which is taken from Carmona et al. (in prep.). $R_{\rm co}$ and $F_{\rm NIR}$, as well as their uncertainties given in parentheses, are measured as explained in Sect. 2. $F30/F13$ values are adopted from Maaskant et al. (2014).

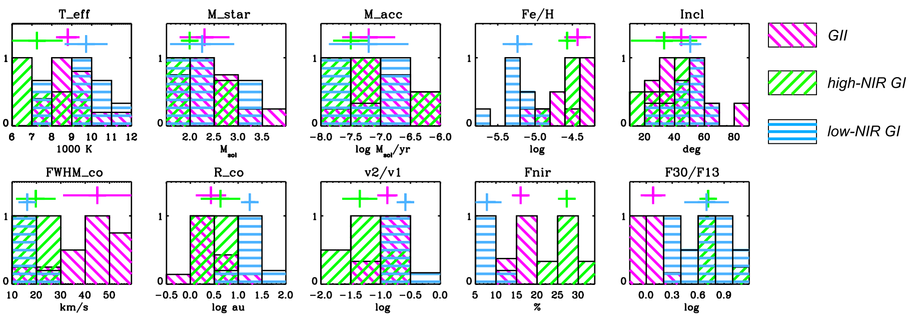

Fig. A.1. Histograms of normalized distributions of the sample parameters included in Table A.1. Median values and median absolute deviations for each category are plotted at the top of each histogram. GII disks are shown in magenta, high-NIR GI disks in green, and low-NIR GI disks in cyan.

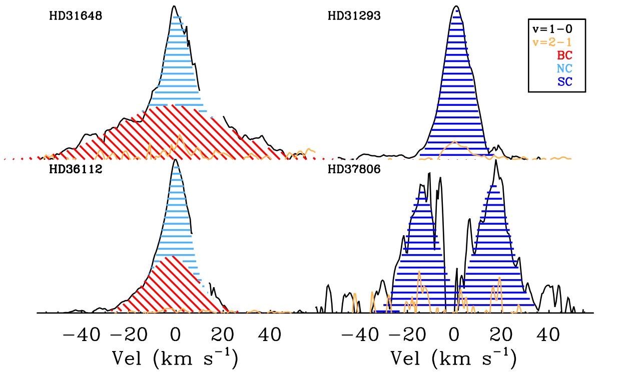

Fig. B.1. Stacked CO lines from the new ISHELL spectra, marking velocity components as in Banzatti & Pontoppidan (2015). HD31648 and HD36112 are the first Herbig disks found with two velocity components, which are typical of T Tauri disks (Banzatti & Pontoppidan 2015).

Appendix B: ISHELL CO spectra

Four disks have been newly observed using IRTF-ISHELL (Rayner et al. 2016) in October 2016 (PI: Banzatti), providing a spectral resolution $R \sim 75\,000$, similar to VLT-CRIRES, which has been used for the other CO spectra. These disks are HD31293 (AB Aur), HD31648 (MWC 480), HD36112 (MWC 758), and HD37806. CO emission is detected in HD37806 for the first time. These spectra were reduced using a set of algorithms developed to reduce data from Keck-NIRSPEC, as described in Brittain et al. (2007), and adapted to ISHELL spectra. For this work, we have stacked the observed line profiles and measured $FWHM_{\rm co}$ as described in Banzatti & Pontoppidan (2015). The stacked lines are shown in Fig. B.1 and can be directly compared to the rest of the CO line profiles published in Banzatti & Pontoppidan (2015) and in van der Plas et al. (2015).

Appendix C: Modeling

We adopted a simple disk model to explore how the NIR excess decreases as a function of the size of an inner dust-depleted disk region. The model is based on physically motivated parameterizations and follows commonly used conventions. Inner disk radius and equilibrium temperature due to stellar irradiation are linked as

$$r = \left(\frac{L_\star}{16\,\pi\,\sigma_{\rm SB}\,T_{\rm d}^4} \frac{C_{\rm bw}}{\epsilon} \right)^{1/2}, \qquad \text{(C.1)}$$

where the ratio of *Planck* mean opacities $\epsilon = \kappa'_{\rm P}(T_{\rm dust})/\kappa'_{\rm P}(T_\star)$ is the dust cooling efficiency. We took $\epsilon = 1$, which is appropriate where the dust is optically thick in the NIR and/or contains a significant amount of particles of size $\gtrsim 1\,\mu$m. $C_{\rm bw} = 4$ is the back-warming factor for optically thick dust, and $4\pi/C_{\rm bw}$ is the spherically integrated solid angle available for cooling (Kama et al. 2009). The gas pressure scale-height is given by

$$h_{\rm gas} = \left(\frac{k_{\rm B}\,T\,r^3}{\mu\,m_{\rm p}\,G\,M_\star} \right)^{1/2}. \qquad \text{(C.2)}$$

The dust rim/wall has a surface area $A = 4\pi\,r\,H_{\rm h}\,h_{\rm gas}$, where $H_{\rm h}$ is a scalar factor specifying where the radial $\tau = 1$ surface is reached in units of gas scale-height. We adopted $H_{\rm h} \sim 3$, in agreement with the height of the radial $\tau = 1$ surface for stellar photons in the Monte Carlo radiative transfer and hydrostatic equilibrium models in the MCMax code (Min et al. 2009; Kama et al. 2009).

The dust rim/wall contributes

$$L_{\rm w} = A \int_{c/5\,\mu{\rm m}}^{c/1\,\mu{\rm m}} B_\nu {\rm d}\nu \qquad \text{(C.3)}$$

to the near-IR excess. Beyond the rim, the disk surface is heated by the stellar flux modulated by the factor $\sin(\beta)$, with β the angle between the ray and the local slope of a flared disk surface. The local thermal balance and luminosity are analogous to the above, and the area per radial cell is $A_{\rm r} = 2\pi r {\rm d}r$. The near-IR luminosity from the disk surface is

$$L_{\rm s} = \int_{r_{\rm w}}^{r_{\rm out}} 2\pi r \int_{c/5\,\mu{\rm m}}^{c/1\,\mu{\rm m}} B_\nu\,[T(r)]\,{\rm d}\nu\,{\rm d}r \qquad \text{(C.4)}$$

and the total NIR luminosity is $L_{\rm w} + L_{\rm s}$.

We explored $F_{\rm NIR}$ as a function of dust radius $R_{\rm dust}$ by increasing the inner rim radius in the model, as illustrated in Fig. C.1. $F_{\rm NIR}$ can be almost constant for small inner holes because of the balance between the increase in surface emitting area and the decrease in temperature. For larger inner holes, the temperature decreases faster than the surface area increases, and $F_{\rm NIR}$ drops.

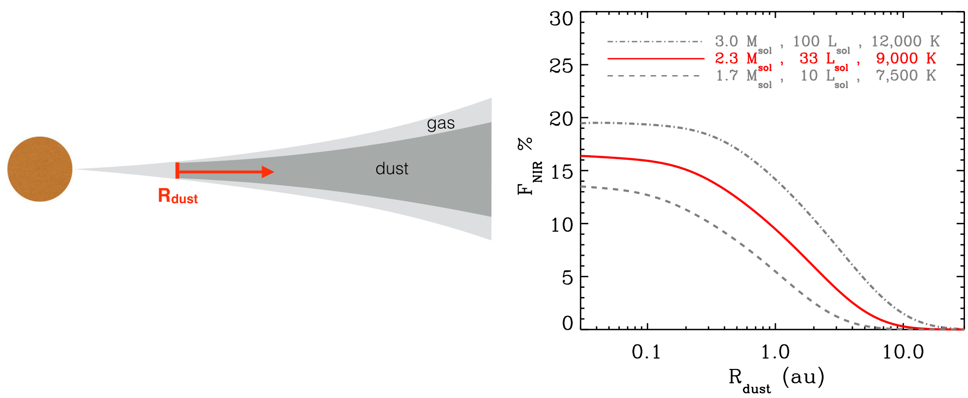

Fig. C.1. *Left:* illustrative cartoon of our simple modeling of inner holes with increasing size. *Right:* model dependence on stellar properties. In the reference model we take median stellar values for the sample (show in red, and reported in Fig. 1). For comparison, we include two representative boundary cases.